Journal of Power Sources 196 (2011) 10601–10605

Contents lists available at SciVerse ScienceDirect

Journal of Power Sources

journal homepage: www.elsevier.com/locate/jpowsour

Short communication

Quantitative analysis of micro structural and conductivity evolution of Ni-YSZ anodes during thermal cycling based on nano-computed tomography

Yong Guan[a,b], Yunhui Gong[c], Wenjie Li[a,b], Jeff Gelb[e], Lei Zhang[d], Gang Liu[a,b], Xiaobo Zhang[a,b], Xiangxia Song[a,b], Changrong Xia[d], Ying Xiong[a,b], Haiqian Wang[c,*], Ziyu Wu[a,b], Yangchao Tian[a,b,**]

[a] National Synchrotron Radiation Laboratory, University of Science and Technology of China, Hefei, Anhui 230029, People's Republic of China
[b] School of Nuclear Science and Technology, University of Science and Technology of China, Hefei, Anhui 230029, People's Republic of China
[c] Hefei National Laboratory for Physical Sciences at Microscale, University of Science and Technology of China, Hefei, Anhui 230026, People's Republic of China
[d] Materials of Science and Engineering, University of Science and Technology of China, Hefei, Anhui 230026, People's Republic of China
[e] Xradia Inc., 4385 Hopyard Road, Suite 100, Pleasanton, CA 94588, USA

ARTICLE INFO

Article history:
Received 21 July 2011
Received in revised form 19 August 2011
Accepted 19 August 2011
Available online 26 August 2011

Keywords:
Anode
Thermal cycles
Ni agglomeration
Microstructure evolution
Nano-computed tomography

ABSTRACT

Understanding the mechanism of degradation in solid oxide fuel cells (SOFCs) using nickel/yttria-stabilized zirconia (Ni-YSZ) as the anode material is very important for the optimization of cell performance. In this work, the effects of thermal cycling on the microstructure of the Ni-YSZ anode are explored using the three-dimensional X-ray nano computed tomography (nano-CT) imaging technique. It is found that the average Ni particle size increased with thermal cycling, which is associated with the decreased connectivity of the Ni phase and the three-phase-boundary (TPB) length. Moreover, the conductivities of the anode samples are also reduced with the increase in thermal cycle times. The implication of these observations is discussed in terms of the relationship between the conductivity and connectivity of the Ni phase.

1. Introduction

In recent years, much attention has been paid to fuel cells because of their ability to produce clean and efficient energy by directly converting chemical energy into electricity. A solid oxide fuel cell (SOFC) uses a hard ceramic electrolyte and operates at very high temperatures, between 500 and 1000 °C, where good ionic conductivity occurs. The electrolyte is usually yttria-stabilized zirconia (YSZ), which conducts oxygen ions but not electrons. SOFC anodes also require an electronic-conducting phase, for which Ni is typically matched to YSZ. The electrodes are porous, enabling the transport of gasses along with ions and electrons. Chemical reactions take place where the ionic, electronic, and gas-conduction phases meet, which are called the triple-phase boundaries (TPBs).

Commercial applications of SOFCs for stationary power sources require their stable performance over long periods of time (>40,000 h); therefore, SOFCs must exhibit mechanical, thermal, chemical, and electrical stability during long-term high-temperature operation. Unfortunately, the electrochemical performance of SOFCs is inevitably degraded during the cell lifetime [1,2]. It is therefore of great importance to understand the degradation mechanism of SOFCs to improve the operation time and optimize the performance. Numerous degradation mechanisms for the Ni-YSZ anode have been proposed [3,4], and among them a prevailing interpretation is the rearrangement and coarsening of the Ni phase [5,6]. If the Ni phase is not stable during operation, the functions of the Ni phase, such as providing a high amount of TPBs for electrochemical reactions, can be significantly altered. It is difficult to define the effect of local conditions such as temperature on any degradation mechanisms [7]. Alternatively, high-temperature thermal-cycling experiments in conjunction with microstructural analysis on the Ni-YSZ anode provide a means of examining the changes in the Ni-YSZ anode under a defined condition. To this end, three-dimensional (3D) information regarding the full pore networks of the anode is desired because it plays a crucial role in modeling, simulating and establishing the correlation between anode microstructure and electrical properties of an SOFC. Recently, the 3D microstructure of SOFC electrodes has been directly measured by scanning electron microscopes equipped with a focused-ion beam (FIB-SEM) [8–12]. By applying these 3D

* Corresponding author.
** Corresponding author at: National Synchrotron Radiation Laboratory, University of Science and Technology of China, Hefei, Anhui 230029, People's Republic of China. Tel.: +86 551 3601844; fax: +86 551 5141078.
E-mail addresses: hqwang@ustc.edu.cn (H. Wang), ychtian@ustc.edu.cn (Y. Tian).

0378-7753/$ – see front matter © 2011 Elsevier B.V. All rights reserved.
doi:10.1016/j.jpowsour.2011.08.083

Table 1
Summary of key parameters calculated from 3D reconstructions of anodes and conductivity measured by four-point probe.

	Non-cycle	2 Cycles	4 Cycles	6 Cycles	8 Cycles
Volume size (μm^3)	283 ± 23	391 ± 32	235 ± 23	434 ± 17	365 ± 37
Surface area of Ni (μm^{-1})	1.65 ± 0.05	1.32 ± 0.06	1.20 ± 0.05	1.15 ± 0.10	1.05 ± 0.04
Surface area of YSZ (μm^{-1})	2.53 ± 0.08	2.90 ± 0.04	2.55 ± 0.06	2.52 ± 0.16	2.21 ± 0.02
Connectivity of YSZ phase (%)	98.3 ± 0.7	98.8 ± 0.2	98.2 ± 0.1	98.8 ± 0.5	99.0 ± 0.1
Connectivity of Ni phase (%)	98.3 ± 1.0	93.9 ± 0.6	93.1 ± 0.5	92.0 ± 1.2	90.6 ± 1.3
Conductivity ($S\,cm^{-1}$)(800 °C)	611	600	550	451	396

measurements, the key microstructural parameters, such as TPB length and tortuosity factors, can be obtained.

In recent years, the development of X-ray optics has allowed the resolution of X-ray microscopy to reach the nanometer range [13,14]. This advancement, coupled with the penetrating power of X-rays, can be applied to examine the 3D volumes of SOFCs that are tens of microns in thickness with spatial resolution on the order of tens of nanometers. Compared to the FIB-SEM technique, nano-CT is a time-saving and non-destructive process for the study of SOFC microstructure. These advantages have made the nano-CT a technique of growing importance in the investigation of the shape, size, distribution and elemental composition of a wide variety of materials [15–18], particularly those used in SOFCs [19–22]. In our previous studies, we utilized X-ray absorption edge spectroscopy to identify the spatial distribution of the constituent Ni, YSZ and pore phases for a composite anode and determined some key microstructural factors that may be linked to the performance of porous composite anodes [23]. Here, the absorption edge analysis technique has been used to study the 3D structural evolutions of Ni-YSZ anodes under thermal cycling without the electrical load. The results are helpful in generating a unique understanding of the microstructure and properties of anodes during heat cycling.

2. Materials and experiments

2.1. Sample preparation

The sample used in this study was taken from the anode used in the SOFC which was consisted of a thin yttria stabilized zirconia electrolyte layer sputtered onto a thick NiO-YSZ anode support by magnetron sputtering, with a composite cathode of $(La_{0.8}Sr_{0.2})_{0.95}MnO_3$ and YSZ. The porous substrate supporting the anode was fabricated using coarse NiO and YSZ powders (NiO:YSZ = 56:44 wt.%) by tape-casting. The anode was sintered in air at 1400 °C for 5 h, then cooled to 800 °C and finally reduced in an Ar/4% H_2 atmosphere to obtain the Ni/8YSZ cermets. Four samples of Ni-YSZ anode were selected for thermal cycling. The anode was first heated to 750 °C in nitrogen. Then, at the same temperature, hydrogen gas was delivered to the anode samples at 50 ml min^{-1} for 4 h. Then anode was finally cooled down to room temperature under a hydrogen atmosphere. This heating-cooling process was considered one thermal cycle. Four samples having undergone two, four, six and eight thermal cycles, respectively, were imaged; an additional Ni-YSZ anode subjected to no thermal cycling was used for comparison. After the thermal cycle testing we fetch a small part from the anode for imaging and analyzing the microstructure.

2.2. Conductivity measurement

A DC four-point probe was applied to measure the conductivities of the anodes. First, a rectangular sample obtained from the porous anode was measured by the DC four-point probe. The four probes are arranged in a linear fashion, where the two outer probes are connected to a current supply, and the inner probes to a voltage meter. As current flows between the outer probes, the voltage drop across the inner probes is measured. Then the resistance of sample can be measured directly. An expression based the co-linear four-probe (4-probe) method was applied to calculate the conductivity (σ) of samples as follow [24]:

$$\rho = \frac{KH}{L}R \tag{1}$$

$$\sigma = \frac{1}{\rho} = \frac{L}{RKH} \tag{2}$$

where L, K and H are the length, width and thickness of measured sample, respectively, ρ is the resistivity and R is the resistance measured by the DC four-point probe.

2.3. X-ray microscope

An Xradia nanoXCT-S100, full-field transmission X-ray microscope (TXM) utilizing the U7A beamline was used to carry out element-specific 3D imaging at the National Synchrotron Radiation Laboratory. This system based on a synchrotron X-ray source, uses elliptical capillary condensers coupled with zone plate optics to perform absorption contrast imaging from 7 to 11 keV. The details of the schematic experimental setup of this X-ray microscope is described elsewhere [25]. Images of samples were acquired at tilt angles ranging from −90° to +90° at an interval of 1° and then reconstructed into tomograms composed of cubic voxels with side lengths of 58.3 nm. The tomograms underwent subsequent processing for analysis, which will be described in the next section. In this paper, two different locations in each sample were selected for imaging and reconstruction. The average sizes of five samples are summarized in Table 1.

3. Results and discussion

First, each series of tomograms was segmented using simple thresholding to label the Ni, YSZ, and pore phases. This technique has been validated in a previous work, and the details are described elsewhere [23]. The same segmentation and analysis procedures developed in the previous work mentioned above were applied in this study. Some key parameters were calculated using the analysis method, the results of which were used to characterize the samples' microstructures.

From initial observation of the 2D radiographs, the Ni particles appeared to gradually agglomerate with increasing numbers of thermal cycles. When the Ni-YSZ anode sample was not treated by thermal cycling, most of the Ni phase appeared as discrete, separated particles, as shown in Fig. 1a. After six thermal cycles, the Ni particles appeared to have migrated toward each other, as observed by the formation of large, highly absorbing features (Fig. 1b). Fig. 1c and d shows 3D renderings of reconstructions before thermal cycling and after six thermal cycles, respectively, where the red label indicates the Ni phase.

The reconstruction results were further analyzed to assess the evolution of the average sizes of Ni particles. Following the Brunauer–Emmett–Teller (BET) formula $d = 6VS^{-1}$ [10], where d, V, and S are average size, volume and surface area, respectively, the mean diameter of each phase after thermal cycling for various times could be estimated as shown in Fig. 2. Clearly, the average diameter

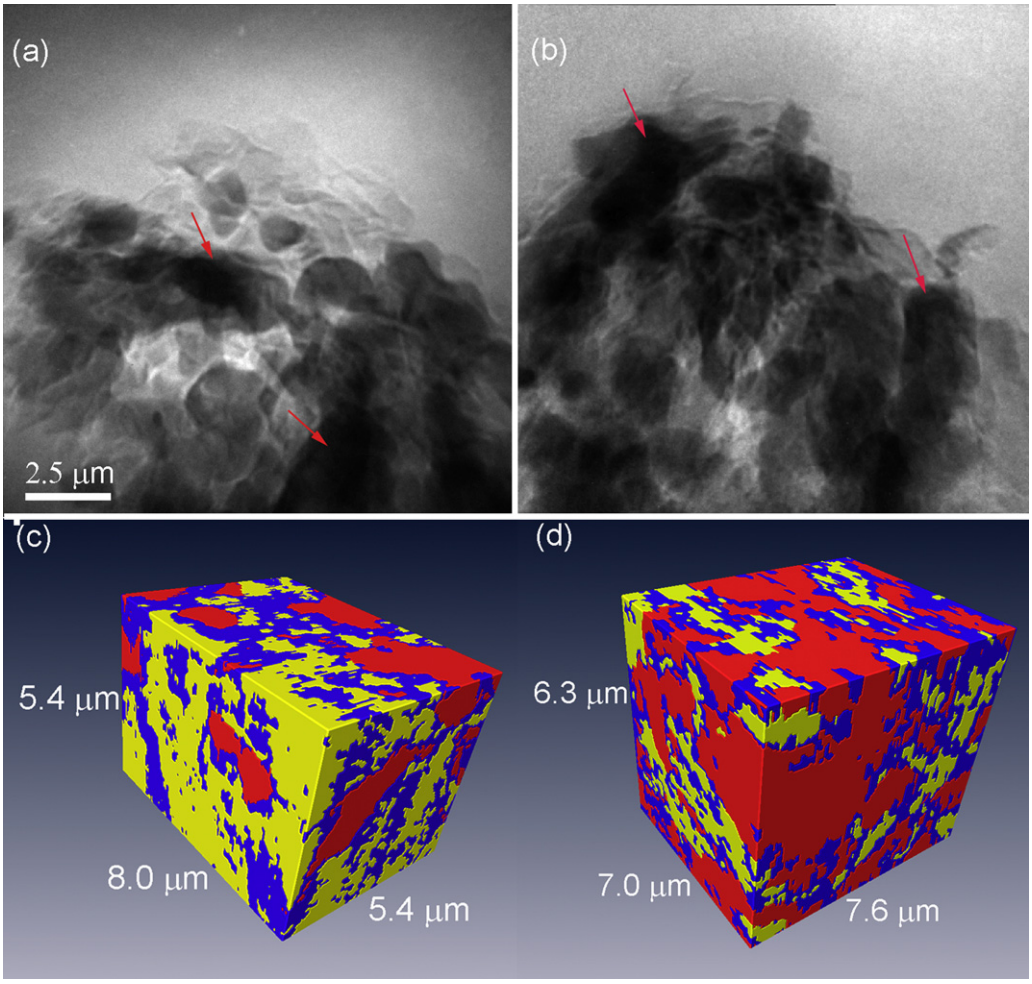

Fig. 1. 2D radiographs of the anode imaged at 8380 eV: (a) non-thermal cycling test and (b) after 6 thermal tests. The regions indicated are the Ni phase. 3D rendering of the (c) non-tested anode and the anode (d) after 6 thermal cycles, where the red is Ni, the blue is YSZ and yellow is pore space.

of the Ni grains increased from approximately 0.86–1.74 μm after eight thermal cycles. Ni grain growth during thermal treatment has been reported by some literature to be dominated mainly by the surface diffusion of Ni atoms on Ni particles [26–28]. This reduction in the surface and grain boundary energies of the material is a driving force for thermally induced microstructural changes. The stability of the YSZ grains, on the other hand, further emphasizes the utility of this material in SOFC anodes. From the data presented here, the YSZ grains did not show a tendency to change like Ni grains, consistent with the results reported by Simwonis et al. [29].

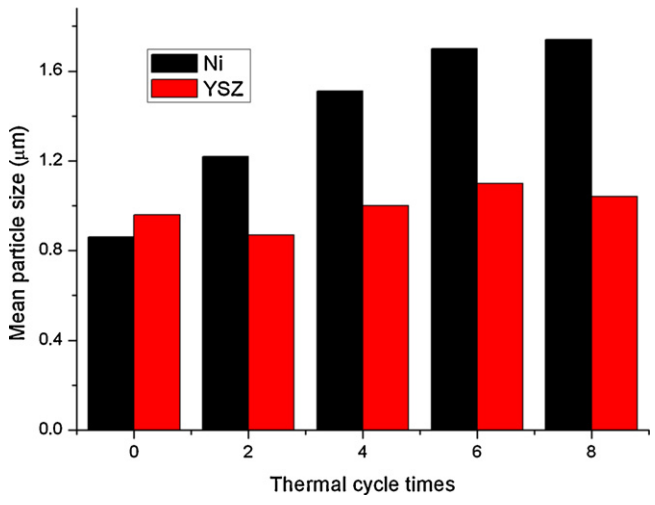

Fig. 2. Evolution of mean particle size with thermal cycle time.

Ni phase agglomeration can also result in the change in the surface Ni phase and interfacial area after thermal cycling. Based on the 3D reconstructed data of the anode samples, the surface area of the Ni and YSZ phase was calculated to demonstrate the Ni phase migration caused by high temperatures. Table 1 presents the variation in the surface area per unit volume during thermal cycling. The surface area per unit volume of the Ni phase decreased from 1.65 to 1.05 μm^{-1} after eight thermal cycles. Meanwhile, the surface area per unit volume of YSZ did not change dramatically during thermal cycling, having been reduced from 2.53 to 2.21 μm^{-1} after eight cycles. The surface area of the YSZ phase remained approximately constant during high-temperature treatment. The changes in the surface area of Ni in this study were similar to those reported in a former study by Thydén [30]. Table 1 also demonstrates that the surface area of Ni decreases significantly after two thermal cycles and that the reduction rate is reduced upon further cycling. It is thus concluded that primary Ni migration and agglomeration occurs during initial operation and may stabilize over time.

The TPB length is also known to have a great influence on cell performance [31,32]; indeed, a long TPB length is beneficial for high electrochemical performance. Thus, it is necessary to investigate the variation of TPB length during high-temperature treatment and then understand the mechanism related to changes in cell

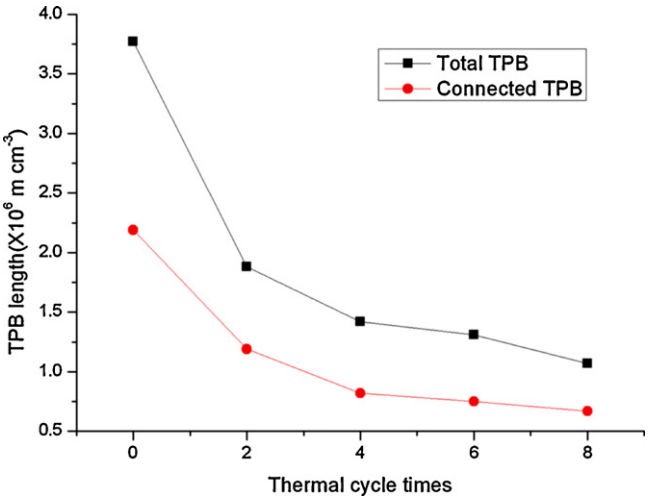

Fig. 3. The total and connected TPB length versus the thermal cycle time.

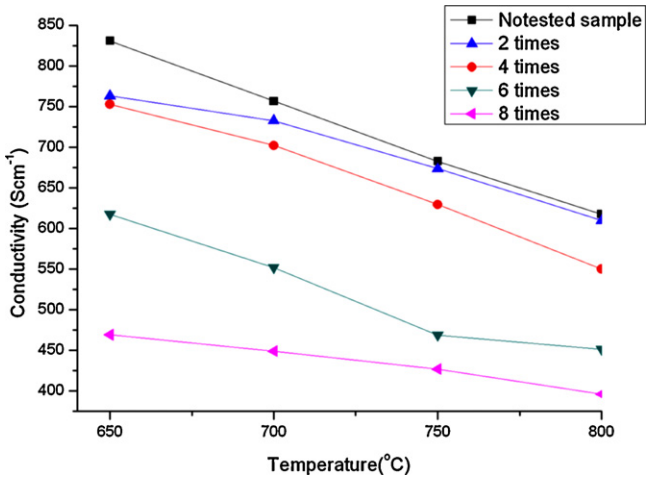

Fig. 4. Variation of conductivity with increasing thermal cycle time and the relationship between the conductivity of anode samples and temperature.

performance. As discussed above, thermal cycling causes substantial microstructural changes, which undoubtedly influence the TPB length. There are two parameters that concern the TPB length of the anode: the total TPB length and the connected TPB length. In this paper, we quantitatively investigated these two parameters of anodes under thermal cycling. Analyses of the variation in the TPB length based on the 3D volume data were performed to investigate the cause of degradation. Fig. 3 shows the variation trends of the TPB and the connected TPB length of the tested anodes after various thermal cycles. One can observe a pronounced decrease (by about 68.2%) of the total TPB length for the anode after eight thermal cycles relative to the anode having undergone no thermal cycling. However, the total TPB length is not the whole story because TPBs must lie on fully connected phases for electrochemical reactions to occur. The connected TPB length was then calculated by including only TPBs located at the boundary connecting Ni, YSZ and pore phases, as shown in Fig. 3. For the non-cycled anode, analysis of the data indicates that 65% of the total TPBs was interconnected, measuring 2.19×10^{12} m^{-2}. The connected TPB of the anode after eight thermal cycles was 0.67×10^{12} m^{-2}. Previous theoretical modeling results [33] have also demonstrated that Ni agglomeration leads to a decrease of the amount of TPBs. A decrease in connected the TPB length will increase the polarization resistance of the electrode and further affect the electrode performance.

It is well known that in the Ni-YSZ anode, the Ni metal phase provides the required electronic conductivity and catalytic activity, whereas the YSZ ceramic phase offers a conduction path for oxide ions. Thus, the connectivity of Ni and YSZ is believed to be of great relevance to the conductivity of the anode. To examine the effects of Ni agglomeration on the connectivity of the anode samples, we calculated the connectivity of each phase upon thermal cycling for different times, as shown in Table 1. The calculated data reveal that 94.4% of the Ni phase in the anode before the thermal cycling was connected. However, it was found that the connectivity of the Ni phase gradually became worse with an increasing number of thermal cycles. After eight thermal cycles, the connected Ni content in the anode sample dropped to 90.6%. Meanwhile, the fluctuation in the connected YSZ phase was small. This revealed that the microstructure of the YSZ phase remained relatively steady during thermal cycling. The decrease in the connectivity of the Ni phase can influence electron conduction; thus the conductivity, as an important parameter for anode operation, may change and was worth studying.

In this study, the conductivity of samples containing non-tested and tested anodes was measured over a temperature range between 650 and 800 °C as shown in Fig. 4. The measured conductivity was mixed, including both electrical and ionic conductivities. It is already understood that the conductivities of all anodes will decrease with increasing from 650 to 800 °C, due to the decrease in the metallic conductivity of Ni with increasing temperature [29]. However, after thermally cycling, the anodes possessed different conductivities at the same temperature For example, the conductivity of the non-cycled anode was 607.7 S cm^{-1} at 800 °C, which dropped to 550.31 and 396.3 S cm^{-1} after four and eight thermal cycles, respectively. It can be found that the conductivity does not decrease immediately and is a function of cycle times. The reduction in conductivity with thermal cycling should be caused by the connectivity of Ni phase in the anode. It is well known that the Ni and YSZ phases in the anode play a role in transmitting electrons and ions, respectively. Thus the connectivity of the Ni phase or YSZ phase is very important for electrical conduction. Table 1 shows the change in conductivity with the decrease in connectivity of the Ni phase at 800 °C, indicating that the decrease in conductivity is likely caused by the reduction in the Ni phase connectivity. It can be deduced that the reduction in the connectivity of the Ni phase during thermal cycling led to the decrease in the conductivity. This is consistent with the results obtained by Lee et al. [34], who also found that the electrical conductivity of the Ni-YSZ anode was a function of Ni phase connectivity and increased as the Ni phase connectivity increased.

4. Conclusions

The studies presented here demonstrate the utility of non-destructive 3D imaging in quantifying and understanding the changes and performance of Ni-YSZ anodes during thermal cycling. The agglomeration of nickel particles was observed in Ni-YSZ anodes after multiple thermal cycles. Due to Ni migration during thermal treatment, agglomeration of the nickel particles occurred, which was also observed in previous studies [35,36]. The agglomeration of the nickel particles resulted in changes in the anode microstructure, such as those in the average Ni diameter, TPB length and connectivity of the Ni phase. The decrease in the connected TPB length may lead to poorer performance due to a decrease in the number of electrochemically active sites [35]. By measuring the conductivity of all of the samples studied in this paper, it was found that the conductivity decreased during thermal cycling. Thus, it can be deduced that the conductivity is correlated with the connectivity of the Ni phase.

Acknowledgements

This work was supported by grants from the 985 project of the State Ministry of Education, the National Natural Science Foundation of China (No. 10734070), and the Knowledge Innovation Program of the Chinese Academy of Sciences (KJCX2-YW-N43).

References

[1] Y.C. Hsiao, J.R. Selman, Solid State Ionics 98 (1997) 33–38.
[2] K.V. Galloway, N.M. Sammes, Journal of the Electrochemical Society 156 (2009) B526–B531.
[3] P. Tanasini, M. Cannarozzo, P. Costamagna, A. Faes, J. Van Herle, A. Hessler-Wyser, C. Comninellis, Fuel Cells 9 (2009) 740–752.
[4] A. Faes, A. Hessler-Wyser, D. Presvytes, C.G. Vayenas, J. Van Herle, Fuel Cells 9 (2009) 841–851.
[5] N. Minh, T. Takahashi, Science and Technology of Ceramic Fuel Cells, Elsevier Science B.V., The Netherlands, 1995, 147–164.
[6] H.Y. Tu, U. Stimming, Journal of Power Sources 127 (2004) 284–293.
[7] P. Metzger, K.A. Friedrich, H. Muller-Steinhagen, G. Schiller, Solid State Ionics 177 (2006) 2045–2051.
[8] J.R. Wilson, W. Kobsiriphat, R. Mendoza, H.Y. Chen, J.M. Hiller, D.J. Miller, K. Thornton, P.W. Voorhees, S.B. Adler, S.A. Barnett, Nature Materials 5 (2006) 541–544.
[9] J.R. Wilson, A.T. Duong, M. Gameiro, H.Y. Chen, K. Thornton, D.R. Mumm, S.A. Barnett, Electrochemistry Communications 11 (2009) 1052–1056.
[10] D. Gostovic, J.R. Smith, D.P. Kundinger, K.S. Jones, E.D. Wachsman, Electrochemical and Solid-State Letters 10 (2007) B214–B217.
[11] P.R. Shearing, J. Golbert, R.J. Chater, N.P. Brandon, Chemical Engineering Science 64 (2009) 3928–3933.
[12] H. Iwai, N. Shikazono, T. Matsui, H. Teshima, M. Kishimoto, R. Kishida, D. Hayashi, K. Matsuzaki, D. Kanno, M. Saito, H. Muroyama, K. Eguchi, N. Kasagi, H. Yoshida, Journal of Power Sources 195 (2010) 955–961.
[13] W.L. Chao, B.D. Harteneck, J.A. Liddle, E.H. Anderson, D.T. Attwood, Nature 435 (2005) 1210–1213.
[14] Y.S. Chu, J.M. Yi, F. De Carlo, Q. Shen, W.K. Lee, H.J. Wu, C.L. Wang, J.Y. Wang, C.J. Liu, C.H. Wang, S.R. Wu, C.C. Chien, Y. Hwu, A. Tkachuk, W. Yun, M. Feser, K.S. Liang, C.S. Yang, J.H. Je, G. Margaritondo, Applied Physics Letters 92 (2008) 103119.
[15] A. Tkachuk, F. Duewer, H.T. Cui, M. Feser, S. Wang, W.B. Yun, Zeitschrift Fur Kristallographie 222 (2007) 650–655.
[16] J. Chen, C.Y. Wu, J.P. Tian, W.J. Li, S.H. Yu, Y.C. Tian, Applied Physics Letters 92 (2008) 233104.
[17] W.J. Li, N. Wang, J. Chen, G. Liu, Z.Y. Pan, Y. Guan, Y.H. Yang, W.Q. Wu, J.P. Tian, S.Q. Wei, Z.Y. Wu, Y.C. Tian, L. Guo, Applied Physics Letters 95 (2009) 053108.
[18] C. Patty, B. Barnett, B. Mooney, A. Kahn, S. Levy, Y.J. Liu, P. Pianetta, J.C. Andrews, Environmental Science & Technology 43 (2009) 7397–7402.
[19] J.R. Izzo, A.S. Joshi, K.N. Grew, W.K.S. Chiu, A. Tkachuk, S.H. Wang, W.B. Yun, Journal of the Electrochemical Society 155 (2008) B504–B508.
[20] P.R. Shearing, J. Gelb, N.P. Brandon, Journal of the European Ceramic Society 30 (2010) 1809–1814.
[21] K.N. Grew, Y.S. Chu, J. Yi, A.A. Peracchio, J.R. Izzo, Y. Hwu, F. De Carlo, W.K.S. Chiu, Journal of the Electrochemical Society 157 (2010) B783–B792.
[22] Y. Guan, W.J. Li, Y.H. Gong, G. Liu, J. Gelb, X.B. Zhang, Y. Xiong, Y.C. Tian, H.Q. Wang, Journal of Synchrotron Radiation 17 (2010) 782–785.
[23] Y. Guan, W.J. Li, Y.H. Gong, G. Liua, X.B. Zhang, J. Chen, J. Gelb, W.B. Yun, Y. Xiong, Y.C. Tian, H.Q. Wang, Journal of Power Sources 196 (2011) 1915–1919.
[24] E.J. Zimney, G.H.B. Dommett, R.S. Ruoff, D.A. Dikin, Measurement Science & Technology 18 (2007) 2067–2073.
[25] Y.C. Tian, W.J. Li, J. Chen, L.H. Liu, G. Liu, A. Tkachuk, J.P. Tian, Y. Xiong, J. Gelb, G. Hsu, W.B. Yun, Review of Scientific Instruments 79 (2008) 103708.
[26] X. Mantzouris, N. Zouvelou, D. Skarmoutsos, P. Nikolopoulos, F. Tietz, Journal of Materials Science 40 (2005) 2471–2475.
[27] R. Vassen, D. Simwonis, D. Stover, Journal of Materials Science 36 (2001) 147–151.
[28] A. Tsoga, A. Naoumidis, P. Nikolopoulos, Acta Materialia 44 (1996) 3679–3692.
[29] D. Simwonis, F. Tietz, D. Stover, Solid State Ionics 132 (2000) 241–251.
[30] K. Thydén, Ph.D. Thesis, Fuel Cells and Solid State Chemistry Department, Technical University of Denmark, DK-4000 Roskilde, Denmark, 2008, pp. 1–123.
[31] J. Mizusaki, H. Tagawa, K. Isobe, M. Tajika, I. Koshiro, H. Maruyama, K. Hirano, Journal of the Electrochemical Society 141 (1994) 1674–1683.
[32] K.R. Han, Y. Jeong, H. Lee, C.S. Kim, Materials Letters 61 (2007) 1242–1245.
[33] A. Ioselevich, A.A. Kornyshev, W. Lehnert, Journal of the Electrochemical Society 144 (1997) 3010–3019.
[34] J.H. Lee, H. Moon, H.W. Lee, J. Kim, J.D. Kim, K.H. Yoon, Solid State Ionics 148 (2002) 15–26.
[35] T. Iwata, Journal of the Electrochemical Society 143 (1996) 1521–1525.
[36] H. Itoh, T. Yamamoto, M. Mori, T. Horita, N. Sakai, H. Yokokawa, M. Dokiya, Journal of the Electrochemical Society 144 (1997) 641–646.